Experimental Mechanics (2011) 51:641–652
DOI 10.1007/s11340-010-9435-2

Martensite Strain Memory in the Shape Memory Alloy Nickel-Titanium Under Mechanical Cycling

K. Kim · S. Daly

Received: 6 June 2010 / Accepted: 1 November 2010 / Published online: 9 December 2010

Abstract This paper describes an experimental study of stress-induced martensitic phase transformation in the SMA Nickel-Titanium. The rich local thermo-mechanical interactions that underlie transformation are examined using three-dimensional Digital Image Correlation (strain fields) and infrared imaging (thermal fields). We quantify the complex local interactions between released/absorbed latent heat and the extent of transformation, and explore the characteristics of the phase fronts and the evolution of martensitic volume fraction. We also quantify a strong strain memory in the martensite that forms in the wake of the phase transformation front. The accommodated strain in the martensite will remain constant during loading, even as the existing phase front propagates. There also exists a remarkable strain memory in the martensite that persists from cycle to cycle, indicating that the local elastic stress fields in the martensite are driven by a dislocation structure and martensitic nuclei that largely stabilize during the first loading cycle.

Keywords Shape memory alloy · Nickel-Titanium · Nitinol · Cyclic · Pseudoelasticity · Strain memory

Introduction

Shape memory alloys (SMAs) are a class of metallic alloys that exhibit a unique capability for superelastic deformation (*pseudoelasticity*) and for reversion to a previously defined shape when deformed and then heated past a set transformation temperature (*shape memory effect*). These abilities stem from a reversible displacive transformation between symmetry-related solid states. In the case of pseudoelasticity, transformation occurs between a high-temperature, high-symmetry austenite phase and a low-temperature, low-symmetry martensite phase. Pseudoelastic behavior arises when the material is deformed at a temperature sufficiently above the transformation temperature. During pseudoelastic deformation, a stress-induced austenite (A) to martensite (M) transformation gives rise to the deformation upon loading. However, the martensite is unstable at this temperature and transforms back to the austenite upon unloading, thereby recovering the deformation. Pseudoelastic deformation can result in the recovery of mechanically-induced strains as large as 8% in Nickel-Titanium (Nitinol), a nearly equiatomic SMA that is of particular interest because of its suitability for biomedical and aerospace applications. There have been a number of experimental and theoretical investigations into the thermo-mechanical behavior of Nickel-Titanium since its discovery, but in spite of intensive research, much is still unknown about the mechanisms of deformation and failure in this alloy. This is in part due to the complexity of these mechanisms and the dependence of their response on interconnected factors such as temperature, strain rate, strain range, thermo-mechanical history, texture, and the interactions of these as well as other variations.

Many of the applications of Nickel-Titanium involve its use under transformation cycling. Several factors can influence the behavior of Nickel-Titanium under cyclic loads, including Ni content, heat treatment of the sample prior to testing, temperature and strain rate at which the test is conducted, and initial microstructure, among

K. Kim (SEM member) · S. Daly (✉, SEM member)
Department of Mechanical Engineering,
The University of Michigan,
Ann Arbor, MI 48109, USA
e-mail: samdaly@umich.edu

others [1–11]. The characteristics of the Nickel-Titanium alloy, such as the critical stress required for the onset of martensitic transformation, the accumulated residual deformation, and the amount of hysteresis, are substantially affected by cycling. As the cycle number increases, it has been found that the forward transformation stress and the amount of hysteresis decrease, while the reverse transformation stress stays nearly constant and the strain-hardening rate increases. This effect is generally attributed to the development of dislocations and/or retention of martensitic nuclei [3, 4, 6, 12–15]. Additionally, the total amount of residual deformation increases but the incremental rate of this deformation decreases as the cycling number increases; this effect is related to Nickel content, applied deformation, and the strain rate of the test, among other factors. Strnadel et al. found that a higher nickel content lead to an increased critical stress required for slip, thus suppressing the development of residual deformation [10]. At higher strain rates, the residual deformation is larger and the critical stress for the onset of martensitic transformation decreases more rapidly [11].

Cyclic fatigue resistance has also been found to depend on crystallographic orientation. Gall et al. found that specimens with a large inherent first-cycle hysteresis show poor fatigue resistance versus specimens with small hysteretic loops, and that the permanent strain mechanism is dependent on precipitate size. Interestingly, this indicates that changing the crystallographic texture of polycrystalline Nitinol may be a more effective means of improving its cyclic properties over conventional heat treatment [2]. In a related study, Yawny et al. found that dislocations act as microstructural markers that allow the material to remember its previous stress–strain history, providing another indication of a microstructural memory for martensitic phase transformation during pseudoelastic cycling [16]. Iadicola and Shaw also noted in their 2002 experiments that the transformation pattern seems to reach a ‘steady state’ during repeated cycling [3].

The objective of these experiments is to quantify the extent and location of this strain pattern memory during the hard cycling of pseudoelastic Nickel-Titanium, and to establish a more complete understanding of stress-induced martensitic phase transformation in a thermo-mechanical framework during cyclic loading. In this paper, we present quantitative, three-dimensional spatial maps of real-time deformation during hard cyclic loading (1st, 2nd, 5th, 10th, 25th, and 50th cycles) and corresponding infrared data of the spatial temperature distribution in thin sheets of Nickel-Titanium. We find evidence of a remarkable strain pattern memory present in the martensite phase, both within a single cycle and from cycle to cycle.

Experimental Methodology

Polycrystalline sheets of Nitinol with an alloy composition of 55 wt% Nickel and 45 wt% Titanium were obtained from Nitinol Devices and Components, Johnson and Johnson. The material was cold-rolled by the supplier into a continuous flat strip nominally 63.5×3048 mm long and 254 μm thick. The specimens were processed to have an A_f of approximately 1.8°C in order to ensure that they were fully austenitic when unloaded and that stress-induced martensite occurred upon loading. The initial texture of the austenite in the as-received state is shown in Fig. 1. The initial texture can have a significant effect on the characteristics of the stress-induced phase transformation, including the elastic response, stresses for nucleation and propagation, and accommodated transformation strain. These are generally very complex effects and are still under active investigation by a number of researchers. Differential scanning calorimetry (DSC model TA-Q200) was used to obtain the austenite start and finish temperatures A_s and A_f as shown in Fig. 2. Dog-bone shaped tensile specimens were extracted parallel to the rolling direction of the sheet by electrical discharge machining with the specimen dimensions shown in Fig. 3.

Full-field characterization of the nucleation and propagation of phase fronts was obtained by simultaneous three-dimensional Digital Image Correlation (DIC) and infrared imaging. DIC is an optical method of measuring displacements on the surface of a sample by tracking a random, isotropic, high contrast pattern on the sample surface. In these experiments, the pattern was applied by airbrushing a uniform, thin coat of solid white titanium oxide on the surface, followed by a speckle pattern of carbon black. Patterning was applied with an Iwata Custom Micron B airbrush gun. Although the axial strain is used to track phase transformation, the full three-dimensional surface displacements were obtained in order to increase the

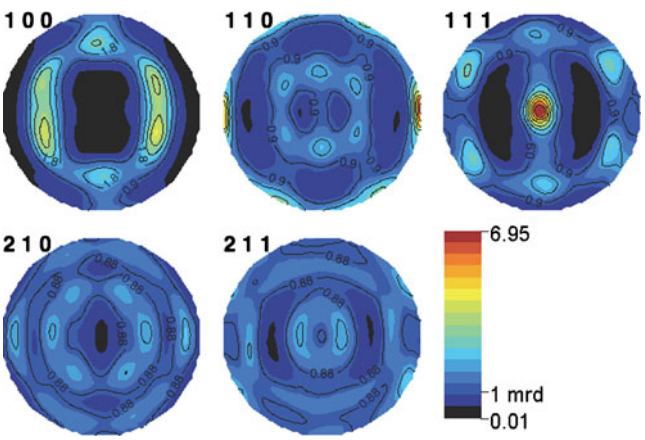

Fig. 1 The texture of the austenite in the as-received state

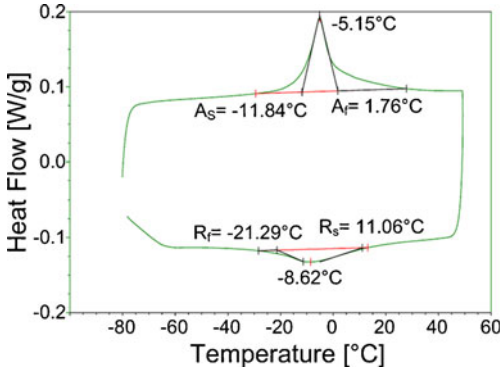

Fig. 2 DSC measurements of the austenite start and finish transformation temperatures

accuracy of the strain field computations through setting the correct reference image, as well as to improve the specimen alignment and to track the degree of bending upon unloading due to the accumulation of residual strain.

The tests were performed on a 45-kip (200 kN) Instron uniaxial electromechanical testing machine with a 1000 lb load cell and a custom LabView-based data acquisition system. Three-dimensional DIC software developed by Correlated Solutions, Inc. was used to calculate the deformation on the surface of the specimen and simultaneous infrared imaging (Inframetrics ThermaCam SC1000) was used to measure the surface thermal fields. The experimental setup is shown in Fig. 4. Two 5-megapixel CCDs (Point Grey GRAS-50S5C) with a spatial resolution of 9.0 μm/pixel were used to image the specimen for digital image correlation, and high shutter speed and light diffuser boxes were employed to improve pattern quality. The samples were tested at $\dot{\varepsilon} = 10^{-4}\text{s}^{-1}$ in zero-to-tension cycling under a ramp profile in displacement control. Samples started in the as-received state and were cycled

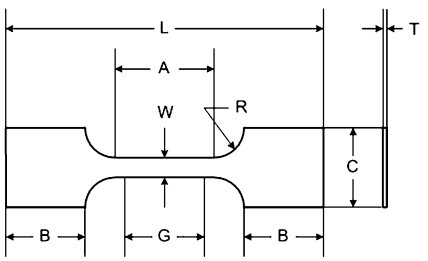

Dimension	mm
G — Gage length	12.5 ± 0.025
W — Width	3.125 ± 0.0625
T — Thickness	0.254
R — Radius of fillet	5
L — Over-all length	50
A — Length of reduced section	15
B — Length of grip section	12.5
C — Width of grip section	12.5

Fig. 3 Tensile specimen dimensions

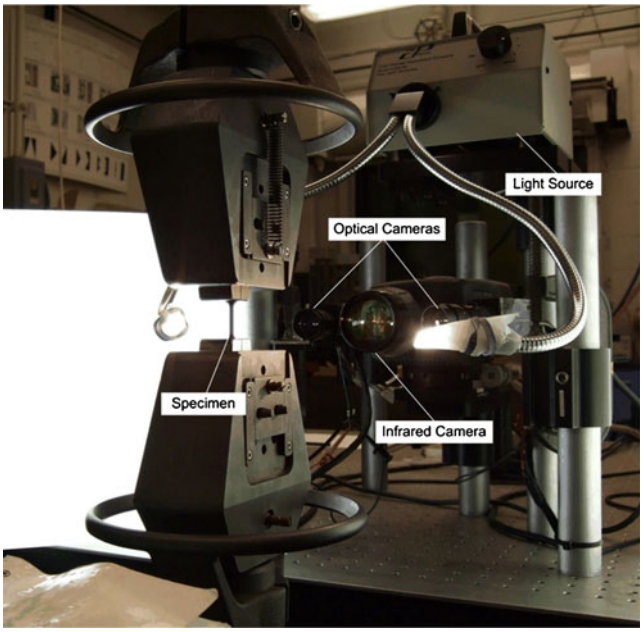

Fig. 4 Experimental setup

50 times. Pattern and rigid body baseline testing were performed to evaluate the accuracy of the setup. The translation error in DIC measurements fell within the error in the load frame applied translation (<0.02 mm) for a range of 0–2 mm, and static error was approximately 0.00025. Using this experimental approach, real-time three-dimensional deformation fields and simultaneous thermal fields were obtained for the evaluation of the spatial development of inhomogeneity and phase transformation fronts.

Results and Discussion

Characteristics of a Phase Front in an As-received Specimen

The macroscopic stress–strain curve for the first cycle on an as-received specimen under a displacement-controlled strain rate of $\dot{\varepsilon} = 10^{-4}\text{s}^{-1}$, along with corresponding strain and thermal images at select points, is shown in Fig. 5. Each data point on the stress–strain curve in Fig. 5 represents a spatial average of the full-field Lagrangian strain map at a point in time obtained by three-dimensional digital image correlation, plotted against the nominal stress applied to the specimen and measured by the load cell at the same moment in time. Snapshots of the specimen were taken after each displacement increment, and the strain distribution in the gage section along the axis of applied load (ε_{YY}) was computed by image correlation. The plotted (ε_{YY}) strain value on the x-axis

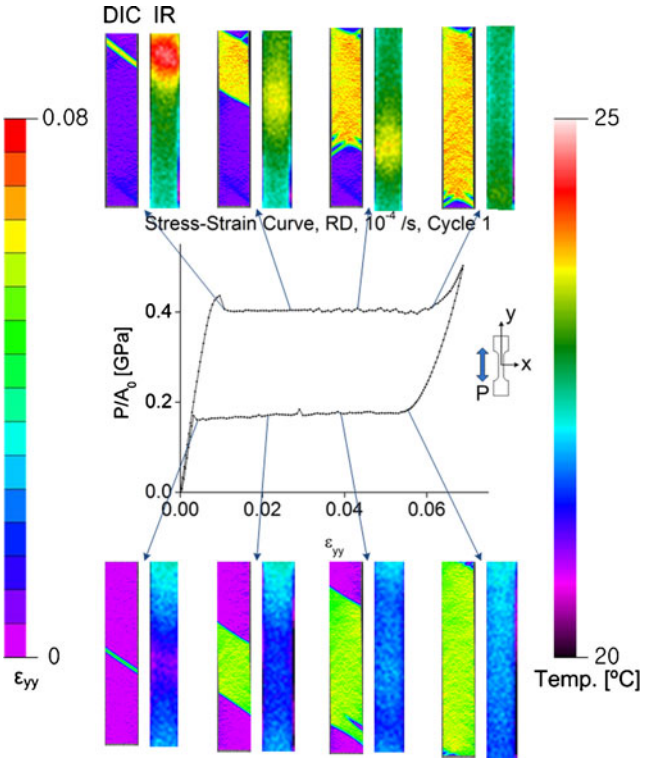

Fig. 5 Stress–strain curve in the gage section of an as-received Nickel-Titanium specimen loaded at $\dot{\varepsilon} = 10^{-4}\text{s}^{-1}$ under displacement control in a ramp profile. The applied stress is obtained from the load cell and the strain along the axis of the specimen, ε_{YY}, is obtained by averaging approximately 600,000 strain values in each DIC image

in Fig. 5 is obtained by an average of approximately 600,000 values over the entire gage section of the specimen. DIC images were triggered and captured directly into LabVIEW with the corresponding load data.

The specimen is macroscopically austenitic at the beginning of the test, behaving in a linear elastic manner with an approximate modulus of 62.3 GPa. The behavior begins to deviate from linearity at $\varepsilon_{YY}\approx 0.007$ for cycle 1. As loading continues, the macroscopic transformation from austenite to stress-induced martensite begins and the curve levels out into a stress plateau. During this transition regime, a localized band of high strain indicating martensitic transformation forms at the top of the specimen and propagates through the gage section. The nucleation and propagation of the martensitic band can be seen in Fig. 5. The band gradually propagates through the entire gage length of the test sample, and the stress begins to increase around a macroscopic strain of $\varepsilon_{YY}\approx 0.063$. Following this, the behavior once again becomes linear with a modulus of approximately 20.5 GPa as the martensite is loaded. This value agrees with prior experimental and numerical investigations into the elastic modulus of stress-induced martensite, which found a range of 14–36 GPa depending on a variety of factors including applied strain rate and temperature [3, 5, 12, 17]. The unloading follows a similar pattern, with an almost linear unloading with a modulus of nominally 35.8 GPa, followed by a departure from linearity at a strain of nominally $\varepsilon_{YY}\approx 0.062$. The stress plateau on unloading is indicative of the reverse transformation from martensite back to austenite, and the localized band accompanying this transformation can be seen through DIC and IR imaging in Fig. 5.

The experimental data in Fig. 5 shows the local self-heating that occurs with the nucleation of the martensitic band, and the relatively quick diffusion of this heat as the band propagates. The initial band nucleation causes a local heat rise of approximately 1.6°C compared with the average temperature in the specimen. Similarly, the final coalescence of the phase front upon unloading causes an approximate 1°C drop in temperature compared with the average temperature in the specimen. In Fig. 6, the local self-heating is examined by considering the simultaneous strain and thermal data down the centerline of the sample. Because there is inherent error in temporally matching the DIC data with the IR data, two IR profiles are shown that are both within this error range. In Fig. 6(a), the strain and thermal data down the centerline of the sample are shown just prior to the formation of a localized martensitic band. There is a small amount of local heating on the side of the specimen where the front will form, but overall the heat is fairly uniform. In Fig. 6(b), the load on the specimen has increased, and the martensitic front has nucleated and propagated through approximately a third of the gage section. In Fig. 6(c), the load on the specimen has further increased and the martensitic phase front has propagated through approximately two-thirds of the gage section. In Fig. 6(d), the specimen has just become fully martensite. In these measurements, one can see that the local temperature maximum slightly leads the martensitic phase front, whose position is clearly visible through the DIC measurements. The resolution of the strain measurements is sub-micron, and is on the order of the grain size ($d<1$ μm) or small clusters of grains. The IR camera has a sensitivity of <0.07° C and an accuracy of 1.2°C. Note that the accuracy of the IR camera, 1.2°C, refers to the difference in the recorded IR temperature as compared with the calibration thermocouple, whereas the camera sensitivity (0.07°C) refers to the resolution in the temperature field as measured by the IR camera. IR images were generated using the Dynamite IR program and analyzed with Matlab.

In Fig. 6(e), the temperature at a fixed point in the center of the gage section of the specimen is monitored as the stress-induced martensitic phase front passes through that location. The discretization of the IR measurements in Fig. 6(e) is 0.3°C, due to interpolation in the dynamite IR program and the value of 60°C set for the temperature span range of the camera. After the phase front has passed

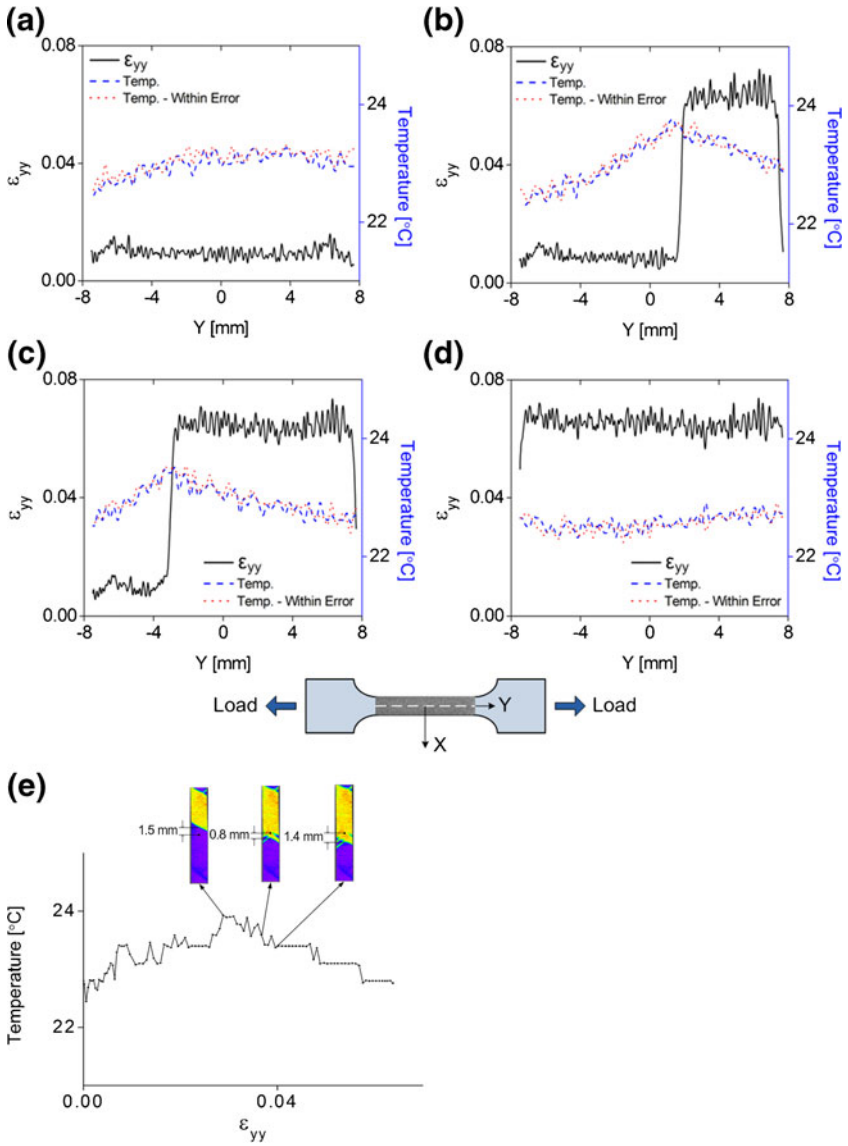

Fig. 6 (**a**-**d**) show the nucleation and propagation of a stress-induced martensitic phase in the gage section of the sample, and corresponding IR data. Data in 6 (a)-6(d) is plotted on a line down the center of the specimen. (**e**) shows thermal data at a fixed point in the center of the specimen as the stress-induced martensitic phase front passes through that location. The lengths (in mm) that are indicated in the middle region of Figure 6(e) are the distances from the fixed point to the phase interface. Both data sets are from the experimental test described in Fig. 5

through the center point, the temperature at this point slowly decreases as shown in Fig. 6(e). The plateaus in the decreasing temperature may be due to the presence of a small martensitic off-shoot branch from the primary phase front, which gradually coalesces; this branch can be seen in the IR images in Fig. 6(e).

Let us take a closer look at the propagation of the stress-induced martensitic phase front in the as-received specimen. As shown in Fig. 7, there exist small branches that nucleate off of the larger martensitic band as the phase front propagates. The nucleation/coalescence of each branch corresponds directly to a small drop/rise in the macroscopic stress–strain curve. For example, point 1 in Fig. 7 corresponds to the nucleation of the primary martensitic band; this drop in stress at nucleation has been widely observed. The primary martensitic band propagates as a single front until point 2, where a small branch occurs on the top right of the front. At point 3 in Fig. 7, the phase front begins to branch out and continues to branch out throughout the remainder of the macroscopic martensitic transformation; this is evident as 'bumpiness' in the macroscopic stress plateau. Branches nucleate at points 3–17 in Fig. 7, and each small branch from the primary transformation front has a corresponding stress drop in the macroscopic stress–strain curve. Similarly, upon unloading, rises in stress correspond to a coalescence of two smaller branches (as shown in Fig. 7, images 20 to 21). It is evident that the single large martensitic phase front propagates through the gage section by the formation of small branches off of the primary martensitic phase front, and that the nucleation and coalescence of these small branches directly affect the macroscopic stress–strain behavior.

The velocity of the phase transformation during loading is shown in Fig. 8(a). Because the transformation front

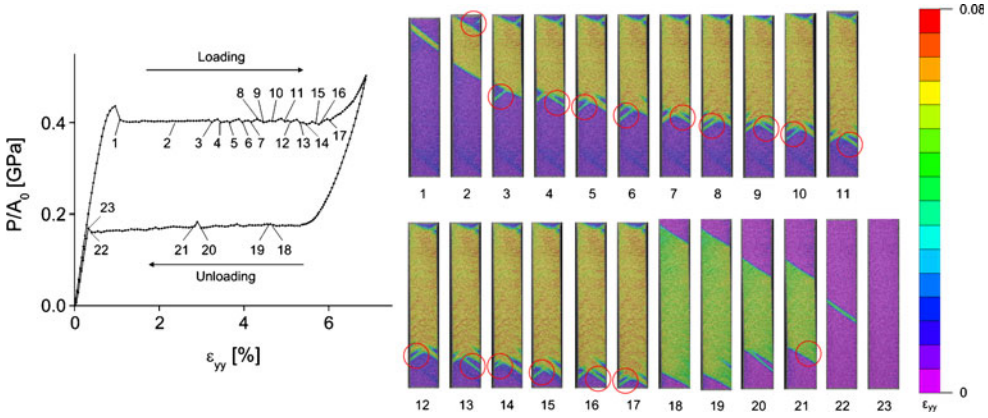

Fig. 7 Detailed images of stress-induced martensitic transformation during the uniaxial tension test described in Figs. 5 and 6. Small branches of martensite appear off of the primary phase front; the nucleation/coalescence of these branches correlates directly with a small rise/drop in the stress. The nucleation of many of these branches in the second half of the plateau cause the latter half of the stress plateau to appear bumpy

branches while it is propagating, it is not appropriate in this case to track the velocity perpendicular to the angled front, because there is no clearly delineated line that remains stable throughout the entire transformation. Instead, the velocity is calculated by tracking the position of the phase front on a line down the center of the gage section of the sample, as shown in the schematic in Fig. 8(a). Thus, the peaks in the velocity data correspond to the nucleation of small branches off of the primary phase front. The front initially propagates as a single line angled approximately 53° to the longitudinal axis of the sample. Small branches then nucleate off of the primary front, changing the phase front from an angled straight line into an inverted "v" shape, as shown in the DIC-calculated images of full-field strain in Fig. 8(a). When a small branch nucleates off the primary front, it can shift the symmetry of this inverted "v," leading to an apparent jump in velocity. In order to make this clear, two images of the phase front used to calculate the velocity are shown for various points in the graph. In Fig. 8(b), the velocity of the phase front upon unloading is shown. Again, due to the appearance of small martensitic branches off of the primary phase front, the velocity is calculated by tracking the position of the phase front on a line down the center of the gage section of the sample, as shown in the schematic in Fig. 8(b).

However, from a strain of nominally $\varepsilon_{YY} = 0.005 - 0.035$ upon loading and unloading, the band propagates as a single phase front with no branching. In Fig. 8(c), this characteristic is exploited to calculate the velocity perpendicular to the angled phase front in the strain range where it is clearly delineated (no branching). Figure 8(c) shows the sum of the velocities of both sides of the martensitic phase front upon loading and unloading in the strain range where there exists a single, clearly delineated phase front. Although the top and the bottom of a single phase front can propagate at substantially different velocities (for example, note in the DIC images of full-field strain in Fig. 5 that upon loading, the top phase front stays relatively still, while it is only the bottom phase front that propagates), the *sum* of the two perpendicular velocities upon loading and unloading is nominally equal, which in this test is at a value of $V \approx 0.04$ mm/s. There are some preliminary indications that the sum of velocities of the phase front faces during loading may tend to be slightly faster than the sum of velocities during unloading; however, a detailed examination of the relationship of phase front velocities, as they depend on texture, strain rate, temperature, and other variables, necessitates an in-depth study and is left to future work.

Pattern Memory

In the macroscopic stress–strain curves shown in Fig. 9(a), the transformation stress decreases with pseudoelastic cycling, in agreement with results from prior work. This effect is generally attributed to local elastic stress fields developed during cycling that are attributed to changes in dislocation structure and/or the retention of martensitic nuclei [6, 13–15]. It is generally known that stress-inducing martensite under mechanical cycling results in a decrease in the forward transformation stress with cycle number, while the reverse transformation stress stays nearly constant. The macroscopic cycling curve produced through spatially averaging DIC images clearly shows this tendency, as well as the characteristic decrease in hysteresis with an increase in cycle number. We observe that the total amount of residual plastic deformation increases, and the rate of accumulation of residual plastic deformation decreases, as cycling increases. These trends in the accumulation of residual plastic deformation are known phenomena that are attributed to the increase in dislocation hardening, and thus the critical stress required for slip, with the increase in cycle number (for example, see [18] and the discussion contained therein).

Figure 9(b) shows the full-field strains in the specimen at the mid-point of transformation for cycles 1, 2, 5, 10, 25 and 50, and Fig. 9(c) shows the corresponding IR-obtained thermal fields. There is sometimes a tendency of the martensitic band to "flip," and to nucleate and propagate from the opposite side of the specimen in a

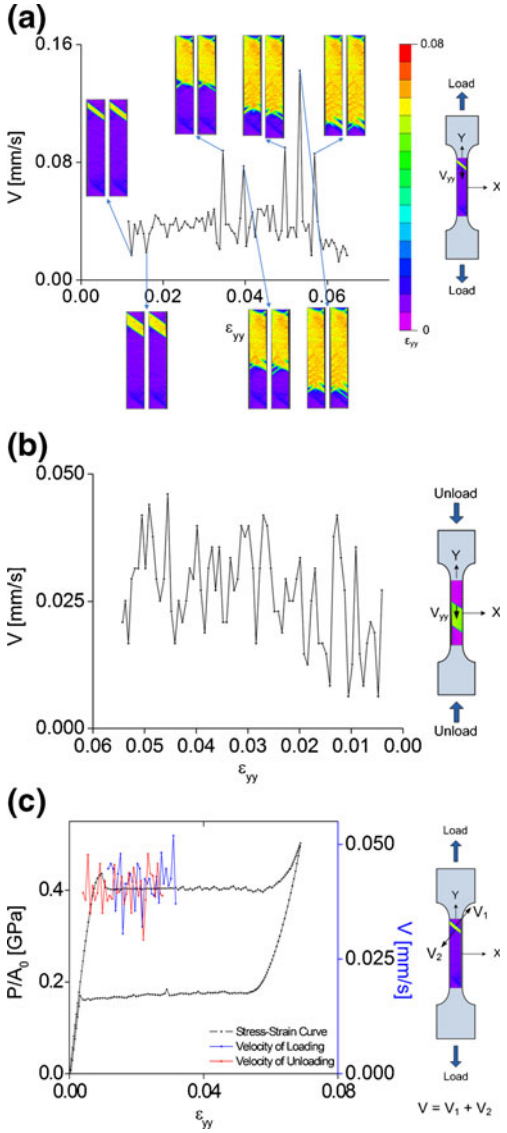

Fig. 8 (**a**) The velocity of the phase transformation during loading in the uniaxial tension test described in Fig. 5. The velocity is calculated by tracking the position of the phase front on a line down the center of the gage section of the sample, as shown in the schematic. (**b**) The velocity of the phase transformation during unloading in the uniaxial tension test described in Fig. 5. The velocity is calculated by tracking the position of the phase front on a line down the center of the gage section of the sample, as shown in the schematic. (**c**) The sum of the velocities of both sides of the martensitic phase front upon loading and unloading in the strain range where there exists a single, clearly delineated phase front (no branching). Although the top and the bottom of the phase front can propagate at different speeds, the *sum* of the two perpendicular velocities is nominally equal, here at a value of $V \approx 0.04$ mm/s

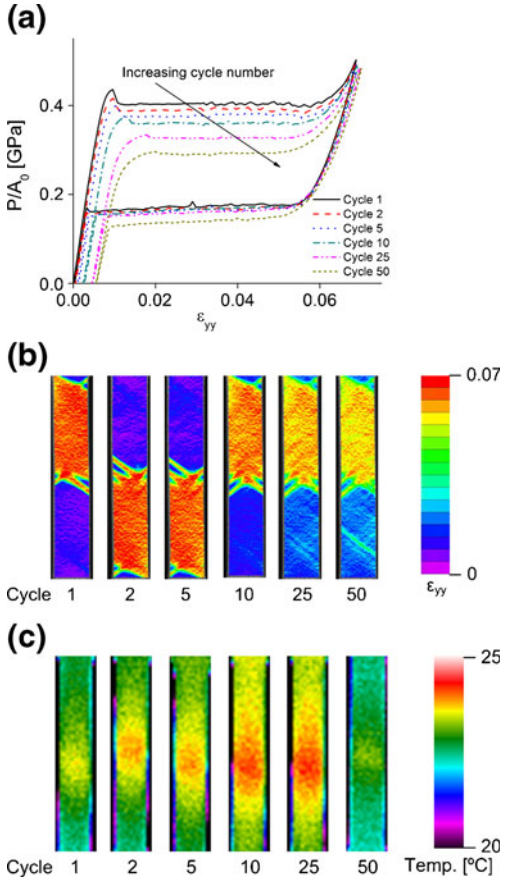

Fig. 9 (**a**) Stress–strain curves in the gage section of an as-received Nickel-Titanium specimen loaded at $\dot{\varepsilon} = 10^{-4}\text{s}^{-1}$ under displacement control in a ramp profile, taken at cycles 1, 2, 5, 10, 25, and 50. The applied stress is obtained from the load cell and the strain along the axis of the specimen, ε_{YY}, is obtained by averaging approximately 600,000 values of ε_{YY} in each DIC image. (**b**) Full-field strains (ε_{YY}) in the specimen at the mid-point of transformation for cycles 1, 2, 5, 10, 25 and 50. (**c**) IR-obtained thermal fields corresponding to the full-field strains shown in (**b**)

subsequent cycle. This occurs more frequently in the earlier cycles. However, even when the martensitic band has flipped to the other side of the specimen, as is the case from cycle 1 to cycle 2, and from cycle 5 to cycle 10 in Fig. 9(b), note that the martensitic phase front keeps the same shape.

As the cycle number increases, the martensitic phase transformation becomes increasingly homogeneous. The number of nucleation sites increases and the delineation of the phase front degrades. However, the degree of positional memory for the bands is very strong; bands tend to nucleate in the same locations, and propagate in the same manner, from cycle to cycle. In order to investigate this tendency for pattern memory, let us examine two situations. In the first case (Fig. 10), the strain on a line down the center of the sample is captured during stress-induced martensitic phase transformation in an as-received specimen. Initially (Fig. 10-i) there is no macroscopic phase front, although the specimen is at a high, relatively uniform strain of 0.0095. The specimen is further loaded and the phase front nucleates and propagates (Fig. 10-ii to iii), and eventually the stress-induced martensitic band has completely propagated through the gage section of the specimen (Fig. 10-iv). What is interesting to note here is that the accommodated

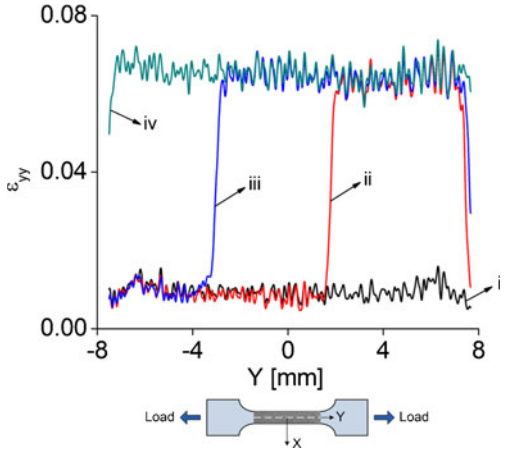

Fig. 10 The strain (ε_{YY}) on a line down the center of the gage section during stress–induced martensitic phase transformation in an as-received specimen loaded at $\dot{\varepsilon} = 10^{-4}\text{s}^{-1}$ under displacement control in a ramp profile. The accommodated strain in the martensite remains the same, even as loading is increased and the phase front propagates

strain in the martensite remains the same, even as loading is increased. For example, the martensite strain profile in Fig. 10-ii closely matches that in Fig. 10-iii, although the loading has increased and the martensitic band has propagated. Even with the increased amount of load and the propagation of the martensitic front, the accommodated strain in the martensite is stable once it has formed.

In the second case, let us examine the axial strain on a line down the center of the sample at the mid-point of martensitic phase transformation, during cycle 1 and cycle 50 (Fig. 11). Figure 11(a) shows the macroscopic stress–strain curves for cycle 1 and 50, and the four points at which the centerline strain profiles are compared (labeled i-iv). These four points correspond to immediately after the large localized band appears (point (i)), during the martensitic band propagation (points (ii) and (iii)), and after the band has finished propagating throughout the gage section (point (iv)). The points between cycle 1 and 50 are chosen when the martensitic band is at the same position in the gage section, determined through the full-field quantitative strain field maps. However, it is interesting to note that this exact choice of points on the macroscopic curve is not necessary in order to see the strain memory effect. The strain memory in the martensite phase is so strong and consistent throughout the loading that it is easily possible to see the strain memory effect using the axial strain profile on quite different points during phase transformation.

Figure 11(b) shows the strain profile at points i-iv in cycle 1, and Fig. 11(c) shows the strain profile at points i-iv in cycle 50. Note the homogenization of the phase transformation as the cycle number is increased. In cycle 1 [Fig. 11(b)], the strain outside the martensitic band stays constant at nominally 0.008 and the strain inside the martensitic band is nominally 0.063. However, by cycle

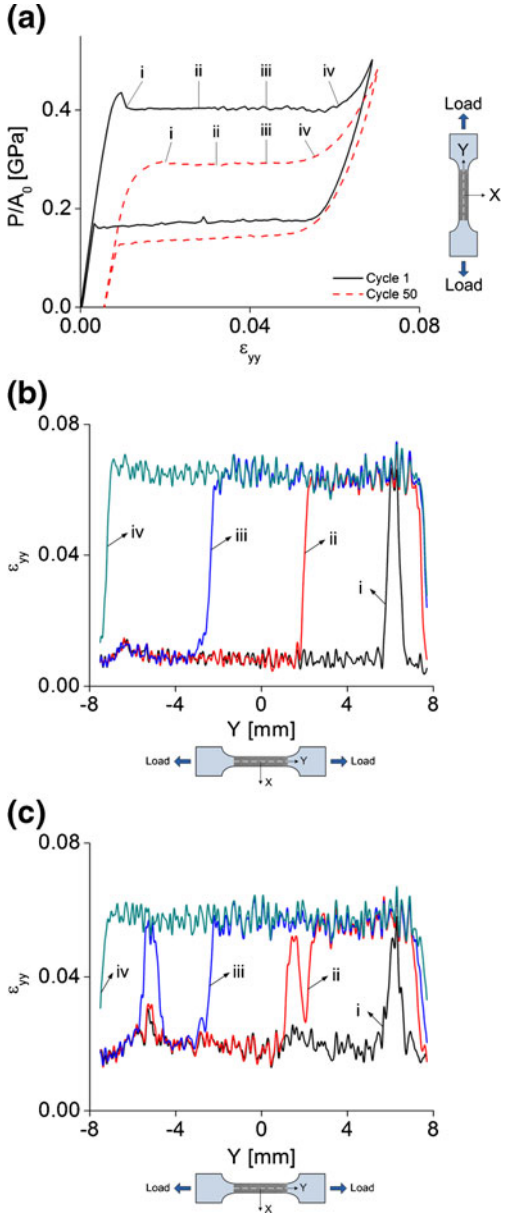

Fig. 11 The axial strain on a line down the center of the sample at the mid-point of martensitic phase transformation, during cycle 1 and cycle 50. (**a**) shows the macroscopic stress–strain curves for cycle 1 and 50, and the points at which the centerline strain profiles are compared (labeled i-iv). (**b**) shows the strain profile at points i-iv in cycle 1, and (**c**) shows the strain profile at points i-iv in cycle 50. Note the homogenization of the phase transformation as the cycle number is increased

50, the strain in the specimen is nominally 0.019 outside the martensitic band, and the strain inside the martensitic band is nominally 0.057. As the number of nucleation sites increases and the phase transformation becomes more homogeneous, the difference in the strain between the inside and outside of the band decreases by 30%, from ~0.055 (cycle 1) to ~0.038 (cycle 50). The increasing homogeneity with cycle number can be attributed in part

to the advantageous formation of dislocation structures and the existence of residual pockets of martensite [6, 10, 11, 19].

The tendency of the strain in the martensite to stabilize within a loading cycle is again evident in Fig. 11(b) and (c). If the strain profiles from cycle 1 and from cycle 50 are now overlaid with each other, there is also clear evidence of strain pattern memory in the martensite from *cycle to cycle* (Fig. 12). To display this cycle-to-cycle martensite strain pattern memory, the strain profiles for cycles 1 and 50 are vertically shifted and compared at various points during the phase transformation (Fig. 11, points i-iv) in Fig. 12. At point i, which immediately follows nucleation, most of the specimen is austenite and there is little pattern memory in the strain field. In Fig. 12(d), the band has completely propagated through the gage section and the specimen can be considered as fully martensite. (Note that although we classify outside the band as macroscopic 'austenite' and inside the band as macroscopic 'martensite,' this is a bit of a misnomer. As is discussed by Brinson et al. [20], martensitic transformation in fact occurs throughout the material at all strain levels, and it is not correct to consider the areas outside the large localized bands as martensite-free, nor the areas inside the large localized bands as completely martensite.) In Fig. 12(d) (fully martensite), the pattern memory between cycle 1 and cycle 50 is quite strong; the strain profiles overlay faithfully with each other. In Fig. 12(b) and (c), mid-way through phase transformation, the strain pattern memory in the martensite is also quite faithful, while again there is significantly less strain pattern memory in the austenite. This finding indicates that the initial manner in which the martensite accommodates strain in the first cycle strongly dictates how the martensite will accommodate strain in future cycles. Thus, one can argue that the local elastic stress fields in the martensite are driven by a dislocation structure and martensitic nuclei that largely stabilize during the first loading cycle [6].

Determination of Martensitic Volume Fraction

The evolution of martensitic volume fraction across the gage section can be estimated from the full-field strain data obtained by DIC. Figure 13(a) shows the macroscopic stress–strain curve for the first loading cycle on the specimen, as described in Fig. 5. Lines of slope E_A (austenite Young's modulus) and E_M (martensite Young's modulus) are offset from the onset and saturation of transformation, respectively, by 0.1% in order to quantify the strains at which macroscopic phase transformation begins and finishes. Thus there are four relevant strains

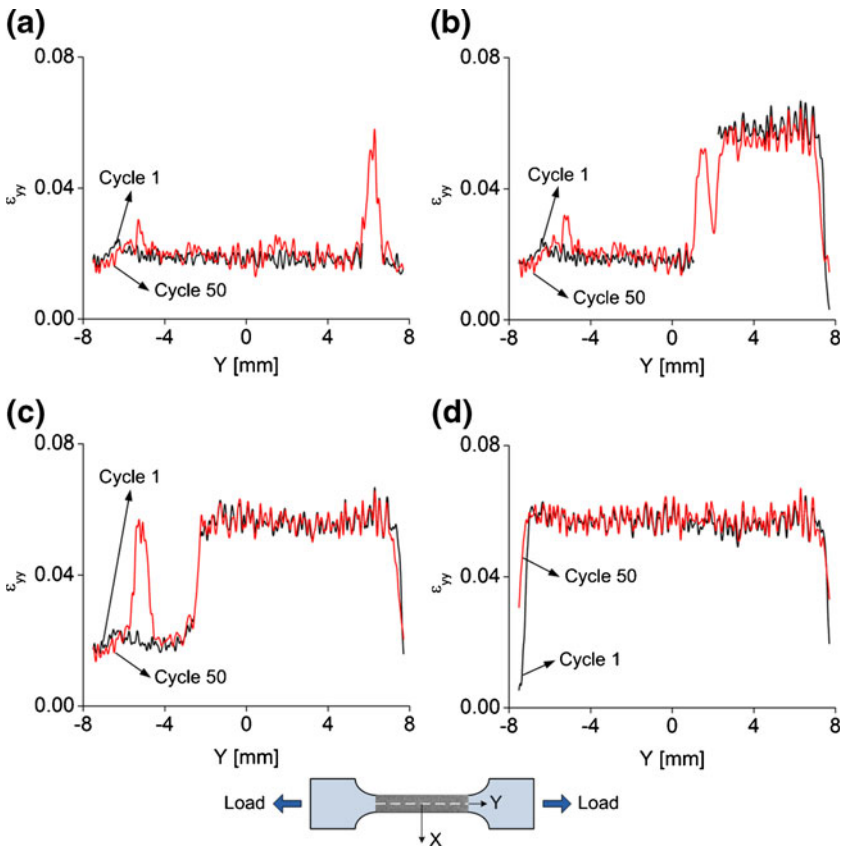

Fig. 12 Overlay of strain profiles from cycle 1 and from cycle 50, where strain profiles are taken on a line down the center of the gage section. There is clear evidence of strain pattern memory in the martensite phase from cycle to cycle. (**a**) overlays the strain profiles for cycles 1 and 50 at point i, which is immediately following nucleation. Most of the specimen is macroscopically austenite at this point, and there is little pattern memory in the strain fields. In Figure 12d, the band has completely propagated through the gage section and the specimen can be considered as fully martensite. Here, the pattern memory between cycle 1 and cycle 50 is quite strong

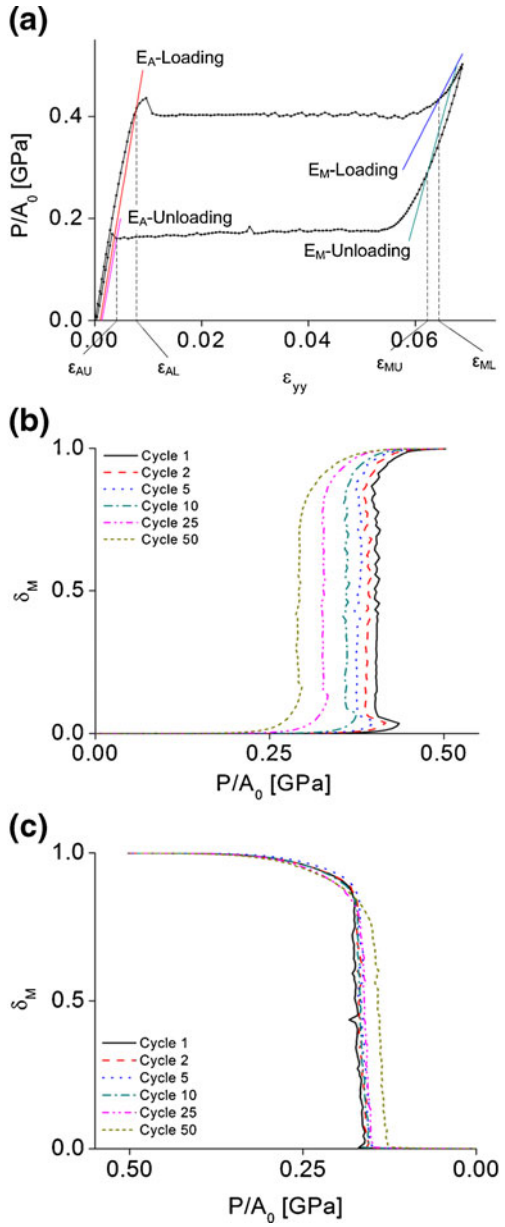

Fig. 13 The evolution of martensitic volume fraction in the gage section during loading and unloading in a sample that is tested in uniaxial tension at $\dot{\varepsilon} = 10^{-4}\text{s}^{-1}$ under displacement control in a ramp profile

for the stress–strain curve at each cycle, which correspond to the offset value for the start of martensitic transformation on loading (ε_{AL}), the finish of transformation on loading (ε_{ML}), the start of transformation on unloading (ε_{MU}), and the finish of transformation on unloading (ε_{AU}). Note that these four representative values need to be determined for any change in loading or sample parameters, such as cycle number, initial texture, or strain rate. Each DIC image in the test is then evaluated in order to determine the extent of martensitic transformation in that image. To evaluate the martensitic volume fraction in a single DIC image, approximately 600,000 points in that image are individually binned using a rule-of-mixtures approach. The overall martensitic volume fraction for the image is taken as:

$$\delta_M = \frac{N_M}{N_{Total}} \tag{1}$$

where N_M is the amount of martensite in all of the pixels, and N_{Total} is the total number of pixels in the image. We consider the number of martensitic pixels as,

$$N_M = M_P + M_T \tag{2}$$

where M_P is the number of pure martensite pixels and M_T is the summed martensitic fraction of the pixels that can be considered as partially martensite. During loading, M_P is defined as the sum of all pixels that have a strain $\varepsilon \geq \varepsilon_{ML}$, and M_T is defined as the sum of the martensitic fraction of pixels that have a strain $\varepsilon_{AL} < \varepsilon < \varepsilon_{ML}$, where

$$M_T = \frac{\varepsilon - \varepsilon_{AL}}{\varepsilon_{ML} - \varepsilon_{AL}} \tag{3}$$

Similarly, during unloading, M_P is defined as the sum of all pixels that have a strain $\varepsilon \geq \varepsilon_{MU}$, and M_T is defined as the sum of the martensitic fraction of pixels that have a strain $\varepsilon_{AU} < \varepsilon < \varepsilon_{MU}$, where

$$M_T = \frac{\varepsilon - \varepsilon_{AU}}{\varepsilon_{MU} - \varepsilon_{AU}} \tag{4}$$

Binning is performed for all the pixels in the image. For a simple example, consider the case where the offset values are ε_{AL}=0.01 and ε_{ML}=0.06, and the strain value of one pixel in a DIC image is 0.03. This single pixel would then, by the rule of mixtures, be binned as 40% austenite and 60% martensite. This procedure is repeated for the nominally 600,000 pixels in each image, and all of the values in each bin are summed in order to determine the final value for martensitic volume fraction (δ_{M}) for that image, taken at a specific point in the loading cycle. This entire procedure is then repeated for each image in the test in order to build up the evolution of δ_{M} as a function of applied stress (P/A_0). This approach results in the quantitative measures of the evolution of martensitic volume fraction shown in Fig. 13(b) (loading) and c (unloading). This method captures the salient features of the evolution of martensitic volume fraction, but there are sources of error that need to be discussed. Firstly, there is possible error in computing the four critical values (ε_{AL}, ε_{ML}, ε_{MU}, ε_{AU}) through the 0.1% offset of linearity method; to create the linear lines in loading and unloading, the linear curve fitting was used with a norm of residuals of 2.4319 MPa. An important error to note comes from the assumption that a pixel is 100% martensite after it contains a strain greater

than ε_{ML}. As shown by previous research and discussed in this paper (for example, see [20] and the references contained therein), it is extremely likely that the pixel still contains a significant amount of residual austenite at strains greater than ε_{ML}. Because each analyzed pixel contains a large number of grains, the amount of residual austenite will be relatively consistent from pixel to pixel with respect to the strain within that pixel. However, it will not be negligible; therefore, what is referred to as 100% martensite or 100% austenite in the evolution of volume fraction should be considered as 100% martensite/austenite as defined by the macroscopic strain, rather than on the microstructural level.

The cycle number has a clear effect on the evolution of δ_M on loading, and substantially less of an effect on the evolution of δ_M upon unloading. This observation agrees with prior macroscopic observations that the reverse transformation stress decreases substantially with cycling upon loading, but stays nearly constant upon unloading. Similar to the macroscopic stress–strain curves, the nucleation or coalescence of bands has a direct impact on the evolution of δ_M, appearing as small but noticeable bumps in Fig. 13(b) and (c).

Conclusions

Simultaneous three-dimensional digital image correlation and infrared imaging were used to examine stress-induced martensitic transformation in Nickel-Titanium during uniaxial, zero-to-tension loading at an applied strain rate of $\dot{\varepsilon} = 10^{-4}s^{-1}$. The effect of hard cyclic loading was examined, particularly the appearance of a strain pattern memory in the martensite both within a cycle and from cycle to cycle. The following was determined:

1. Stress-induced martensitic phase transformation can propagate either by a single, clearly delineated front, or alternatively by the offshoot of small branches from the primary phase front. A single martensitic front can change to a branched front in the middle of phase transformation, as shown in Fig. 5. The nucleation/coalescence of these small branches directly corresponds to a load drop/rise in the macroscopic stress–strain curve.
2. Although the top and the bottom of a single phase front can propagate at substantially different velocities (for example, note in Fig. 5 that upon loading, the top phase front stays relatively still, while it is only the bottom phase front that propagates), the *sum* of the two velocities taken perpendicular to the phase front was found to be nominally equal upon loading and unloading in these tests.
3. The accommodated strain in the microstructure of martensite that has already been formed will remain constant, even as loading is increased and the martensitic phase front propagates through the gage region (Fig. 10).
4. The number of nucleation sites increases and the delineation of the stress-induced martensitic phase fronts decreases as cycle number is increased. However, although the transformation becomes more homogeneous during cycling, there is a remarkable amount of strain pattern memory in the martensite from cycle to cycle. This can be seen in an overlay of the strain values down the centerline of the gage section from the 1st cycle on an as-received specimen and from the 50th cycle on the same specimen, as shown in Fig. 12. Note that the tendency to have strain memory is much stronger in the stress-induced martensite (inside the localized band) than in the austenite (outside the localized band). The initial manner in which the martensite accommodates strain in the first cycle strongly dictates how the martensite will accommodate strain in future cycles. Thus, one can argue that the local elastic stress fields in the martensite are driven by a dislocation structure and martensitic nuclei that largely stabilize during the first loading cycle.
5. By using a rule-of-mixtures approach on the DIC-obtained full-field strains, the evolution of martensitic volume fraction across the gage section of the specimen as a function of the applied load can be examined. The cycle number has a clear effect on the spatial evolution of δ_M on loading, and substantially less of an effect on the spatial evolution of δ_M upon unloading.

By using simultaneous IR and DIC imaging, the rich local thermo-mechanical interactions that underlie martensitic phase transformations can be investigated. Future work will examine the characteristics of individual phase fronts and their dependence on applied strain rate and initial microstructure.

Acknowledgements The authors gratefully acknowledge the financial support of the US Department of Energy, Office of Basic Energy Sciences (contract No. DE-SC0003996 monitored by Dr. John Vetrano), who funded the cyclic experiments and analysis detailed in this paper. The authors also thank the Horace J. Rackham School of Graduate Studies and the University of Michigan for the start-up funding that allowed the initiation of this work in 2009. The authors would like to acknowledge Professor John Shaw for the generous use of his IR camera, and Mr. Benjamin Reedlunn for his experimental assistance. The authors thank Dr. Joel Bernier and Ms. Anne Juggernauth for texture measurements.

References

1. Eggeler G, Hornbogen E, Yawny A, Heckmann A, Wagner M (2004) Structural and functional fatigue of NiTi shape memory alloys. Mat Sci Eng A 378(1–2):24–33

2. Gall K, Maier HJ (2002) Cyclic deformation mechanisms in precipitated NiTi shape memory alloys. Acta Mat 50:4643–4657
3. Iadicola MA, Shaw J (2002) The effect of uniaxial cyclic deformation on the evolution of phase transformation fronts in pseudoelastic NiTi wire. J Intel Mat Syst Str 13(2/3):143–156
4. Lim TJ, McDowell DL (1994) Degradation of an NiTi alloy during cyclic loading. Proc. 1994 North American Conference on Smart Structures and Materials. SPIE, 153–165
5. Matsuzaki Y, Naito H, Ikeda T, Funami K (2001) Thermo-mechanical behavior associated with pseudoelastic transformation of shape memory alloys. Smart Mat Struct 10(5):884–892
6. McCormick PG, Liu Y (1994) Thermodynamic analysis of the martensitic transformation in NiTi-II. Effect of transformation cycling. Acta Metall Mater 42(7):2407–2413
7. Melton KN, Mercier O (1979) Fatigue of NiTi thermoelastic martensites. Acta Metall 27(1):137–144
8. Shaw JA, Kyriakides S (1995) Thermomechanical aspects of NiTi. J Mech Phys Solids 42(8):1243–1281
9. Shaw JA, Kyriakides S (1997) On the nucleation and propagation of phase transformation fronts in a NiTi alloy. Acta Mater 45 (2):683–700
10. Strnadel B, Ohashi S, Ohtsuka H, Ishihara T, Miyazaki S (1995) Cyclic stress-strain characteristics of Ti-Ni and Ti-Ni-Cu shape memory alloys. Mat Sci Eng A202:148–156
11. Strnadel B, Ohashi S, Ohtsuka H, Miyazaki S, Ishihara T (1995) Effect of mechanical cycling on the pseudoelasticity characteristics of Ti-Ni and Ti-Ni-Cu alloys. Mat Sci Eng A203:187–196
12. Entchev PB, Lagoudas DC (2008) Modeling of transformation-induced plasticity in SMAs. In: Lagoudas DC (ed) Shape memory alloys: modeling and engineering applications, 1st edn. Springer Science and Business Media, LLC, New York, pp 233–276
13. Miyazaki S, Imai T, Igo Y, Otsuka K (1986) Effect of cyclic deformation in the pseudoelasticity characteristics of TiNi alloys. Metall Trans 17A:115–120
14. Patoor E, Barbe P, Eberhardt A, Berveiller M (1991) Internal stress effect in the shape memory behavior. J Phys IV 1:C4–C95
15. Sehitoglu H, Anderson R, Karaman I, Gall K, Chumlyakov Y (2001) Cyclic deformation behavior of single crystal NiTi. Mat Sci Eng A 314(1–2):67–74
16. Yawny A, Sade M, Eggeler G (2005) Pseudoelastic cycling of ultra-fine-grained NiTi shape-memory wires. Z Met kd 96(6):608–618
17. Daly S, Ravichandran G, Bhattacharya K (2007) Stress-induced martensitic phase transformation in thin sheets of Nitinol. Acta Mater 55(10):3593–3600
18. Miyazaki S, Otsuka K (1989) Development of shape memory alloys. ISIJ Int 29(5):353–377
19. DesRoches R, McCormick J, Delemont M (2004) Cyclic properties of superelastic shape memory alloy wires and bars. J Struct Eng ASCE 130(1):38–46
20. Brinson LC, Schmidt I, Lammering R (2004) Stress-induced transformation behavior of a polycrystalline NiTi shape memory alloy: micro and macromechanical investigations via *in situ* optical microscopy. J Mech Phys Solids 52(7):1549–1571